AIAA JOURNAL
Vol. 34, No. 3, March 1996

Recirculation Zones of Unconfined and Confined Annular Swirling Jets

H. J. Sheen,* W. J. Chen,† and S. Y. Jeng†
National Taiwan University, Taipei 10764, Taiwan

An experimental study is presented for flowfields behind an axially mounted cylindrical bluff body of annular swirling jet flows. Both the confined and the unconfined cases are examined. The controlled parameters included the Reynolds number *Re* and the swirl number *S*. Smoke streaks were used to observe the dynamic flow structures of the recirculation zone behind the bluff body. Laser–Doppler anemometry was used for velocity measurements at the jet exit and downstream of the annular jet flows. The results indicate that the recirculation zones for both the unconfined and the confined cases can be classified into seven typical flow patterns based on the Reynolds number and swirl number: stable flow, vortex shedding, transition, prepenetration, penetration, vortex breakdown, and attachment. The flow patterns and their domains in (*Re*, *S*) space for unconfined and confined cases were basically the same. In the attachment regime, the central recirculation zone for the confined case was larger than that for the unconfined case. The boundaries of the recirculation zone for various flow conditions were investigated. Scaling analysis was used to correlate the lengths of the recirculation zone with the swirl number.

I. Introduction

BECAUSE of the formation of the recirculating zone and the standing vortex inside the near-wake region, the flame of a turbulent reacting flow in an industrial burner and a gas turbine can be stabilized in the region behind the bluff body.[1,2] The use of a swirling flow obtained from a swirl generator in a combustion chamber also improves the flame stability by means of the formation of a toroidal recirculation zone. Furthermore, the introduction of swirling motion into a jet flow can lead to a higher ambient entrainment flow and can enhance flow mixing, particularly in the shear-layer region. The aerodynamic properties of the swirling flow have been investigated by others.[3,4]

There have been many studies of the effects of bluff body geometry on flow structures. Taylor and Whitelaw[5] studied the velocity characteristics behind various axisymmetric bluff bodies, such as a circular disc and a cone, and the effects of the blockage ratio. They concluded that the recirculation bubble was shorter and narrower for a flow with a 45-deg cone than for one with a disk, and that decreasing the blockage ratio would lengthen and narrow the recirculating bubble. Li and Tankin[6] carried out a flow visualization experiment for isothermal and combusting flows with various axially aligned cylindrical bluff bodies at the exit of an annular jet. The variations of recirculation length in the near-wake region behind the bluff body were discussed, and the asymptotic solutions for the recirculation length were derived. In brief, the recirculating length changed with the flow conditions (e.g., confined or unconfined flows, Reynolds number, and turbulence intensity) and the geometries of the bluff body (e.g., shape, diameter, and blockage ratio). Chan and Ko[7] studied the characteristics of vortex shedding behind an axially aligned axisymmetric centerbody. They found that the presence of the central recirculating region and the wake vortices in the basic annular jet had the effect of accelerating the jet flow into a fully developed state.

Chigier and Beér[8] measured velocity and static pressure in an unconfined swirling annular jet where the degree of swirl was varied by proportions of air introduced axially and tangentially into the swirl generator. They concluded that a closed toroidal vortex was formed behind the central bluff body because of the comparatively large subatmospheric pressure in the near-wake region at sufficiently high degrees of swirl; the strength and size of this vortex increased as the swirl strength increased.

Rhode et al.[9] investigated the effects of a confined boundary on an annular swirling jet with various swirling vane angles and different sidewall expansion angles. Their results showed that increasing the swirling vane angle influenced the formation of a central recirculation bubble, and that this zone length was only slightly affected by the sidewall expansion angle. Concerning the formation of a central recirculation zone behind a bluff body for weak and intermediate swirl cases, Escudier and Keller[10] noted that when the swirl strength was increased, the axial–radial flowfield did not change significantly until a certain critical swirl number was reached, and then an isolated axisymmetric recirculation zone appeared in the downstream region. As the degree of swirl was increased, the recirculation zone moved upstream. When the swirl strength reached a critical level, the wake downstream of the central cylinder and the isolated recirculation zone joined. The so-called isolated recirculation zone is the location of vortex breakdown, which is a vortex flow with abrupt and drastic changes in the axial velocity component. The characteristics of vortex breakdown are commonly recognized as the formation of a stagnation point on the axis and a sudden widening of the vortex core because of a region of reversed axial flow. Some observations about the vortex-breakdown phenomenon were presented by Harvey,[11] Chanaud,[12] and Sarpkaya.[13]

On the basis of background knowledge from previous works, we carried out flow visualization using electrified smoke wires and a miniature smoke generator to study the various flow patterns in the toroidal vortex. Also studied were the dynamic behaviors of the recirculation zone behind an axisymmetric and vertically mounted cylindrical bluff body of annular swirling and nonswirling jets. In this study, the characteristics of several typical flow patterns are investigated for a flow in various ranges of Reynolds number and swirl number. The boundaries of the recirculation zone under various flow conditions are also investigated. The recirculation lengths for various flow conditions are derived analytically, and analytical solutions are compared with the experimental results.

II. Experimental Details

A. Flow Arrangement

The schematic diagram of the experimental setup is shown in Fig. 1. The airstream from two 11-kW (15-hp) air compressors was passed through a dehumidifier filter into a 3.5-m^3 storage tank. This tank was used to eliminate the unstable stroke effect and to ensure a regulated and stable air supply. An air filter and a pressure regulation valve placed at the outlet of the tank were used to clean and control the airflow. A vortex flowmeter for high flow rate and a rotameter for low flow rate measurements also were placed at the storage tank

---

Received Dec. 5, 1994; revision received Oct. 26, 1995; accepted for publication Nov. 16, 1995. Copyright © 1996 by the American Institute of Aeronautics and Astronautics, Inc. All rights reserved.

*Associate Professor, Institute of Applied Mechanics.

†Graduate Student, Institute of Applied Mechanics.

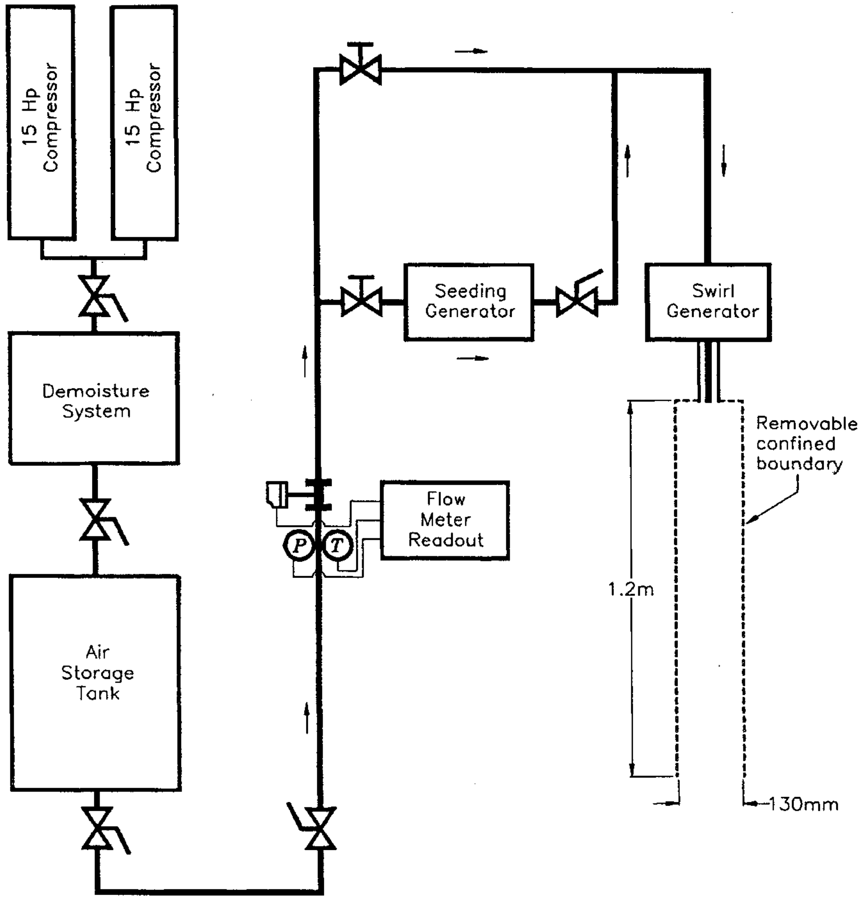

Fig. 1 Schematic diagram of the experimental setup.

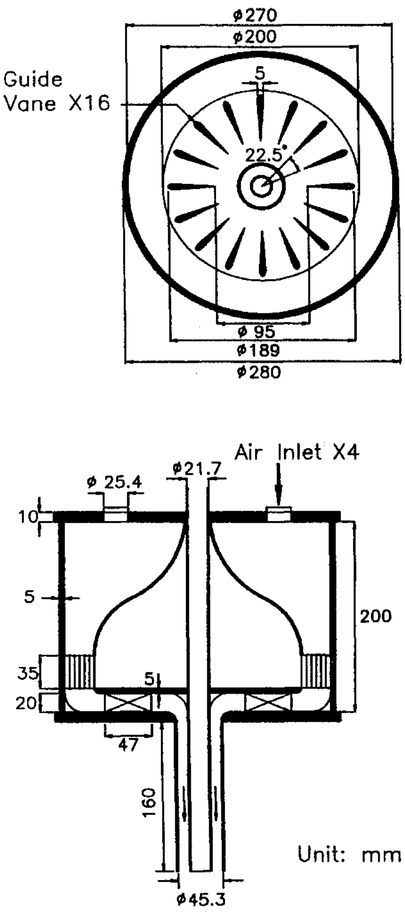

Fig. 2 Schematic diagram of the radial-type swirl generator.

outlet to monitor the airflow. The uncertainty of the airflow rate was estimated to be less than 1%.

The detailed geometry of the radial-type swirl generator is given in Fig. 2. The airflow passed through a curved settling chamber into a 16-guide-vane swirl generator. The angle of the guide vane was controlled by a stepping motor with an angle decoder and could be adjusted from 0 to 56 deg with a resolution of 0.1 deg. The swirling airflow was then sent to the annular test section, which had a concentric cylinder. The annular airflow region had an inner diameter d of 21.7 mm and an outer diameter D of 45.3 mm. For the confined case, a sudden-expansion plexiglass tube with an inner diameter D_E of 130 mm was placed at the exit of the annular pipe (see Fig. 1). The test section was 1.2 m long and the expansion ratio D_E/D was 2.87. Furthermore, the experiments for the unconfined case were carried out with the sudden-expansion tube removed. In this experiment, the coordinates included x for the axial distance from the center of the bluff-body base, r for the radial direction, and θ for the azimuthal direction.

B. Flow Visualization Technique

Smoke was used to visualize the detailed flow patterns of the recirculation zone and the vortex breakdown. Depending on the range of the Reynolds number, smoke wires and a miniature smoke generator were used for $Re < 1500$ and $Re > 1000$, respectively. In the smoke-wire technique, twisted stainless-steel wires with a diameter of 0.1 mm were placed across the center plane of the jet flow to generate smoke streaks for the flow. The Reynolds number based on the wire diameter was kept lower than 13, which was less than the limit of 20 recommended by Mueller.[14] To avoid the influence of the surface temperature of the smoke wire, the power supply was turned off after the vapor of hydrocarbon oil, brush-coated on the wire surface, had been generated. The smoke remained observable inside the recirculation zone for at least 30 s. Thereafter, the flowfield illuminated by a 100-W arc lamp was photographed with a still camera. A video camera was also used to observe the transient phenomena of the flow. The custom-made miniature smoke generator was embedded inside the cylindrical bluff body. Hydrocarbon oil also was used. The vaporized smoke was released from a very narrow slit at the base of the bluff body. A laser sheet, obtained by using a 3-W argon-ion laser and a cylindrical mirror, was applied to provide detailed two-dimensional visualization of the dynamic structures of the recirculating zone. Pictures were taken with a still camera and a video camera. The shutter speed of the still camera was set below 2 ms.

C. LDA System

A four-beam, two-component forward-scattering laser-Doppler anemometry (LDA) system was used for the velocity measurements for the annular swirling and nonswirling jet flows. A 3-W argon-ion laser, with blue and green beam wavelengths of 488 and 514.5 nm, respectively, was used as the light source. The beam space was 50 mm, and the focusing length was 350 mm. Bragg cells were used for both components to extend the measurement range and enable reversed-flow measurement. A beam expander, expansion ratio 2.27, was used to reduce the measuring volume and to increase the signal-to-noise ratio. Two counter-type signal processors with direct-memory-access interface linked to a personal computer were used for data acquisition.

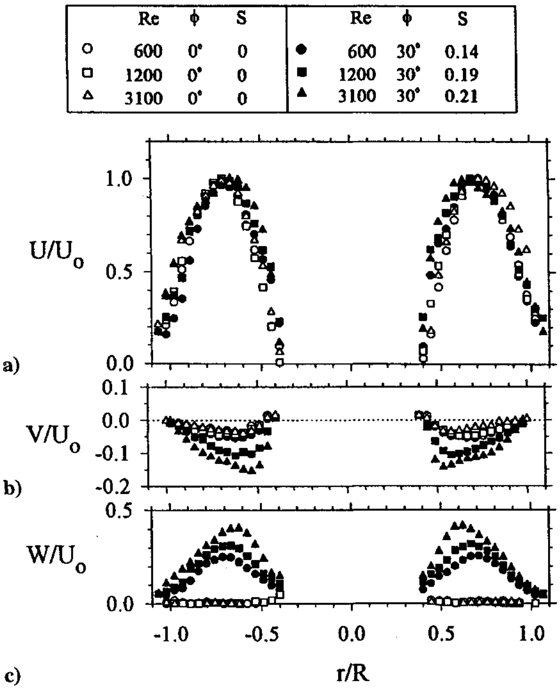

Fig. 3 LDA measurements of the mean-velocity profiles at the jet exit (x/D = 0.09): a) axial velocity, b) radial velocity, and c) azimuthal velocity.

The LDA system was mounted on a computer-controlled X-Y-Z traversing system for measurement position adjustment. The precision of the traversing system was 25 μm for the Y and Z axes, and 2.5 μm for the X axis. In this experiment, the uncertainty for LDA velocity measurements was estimated to be less than 3%.

D. Velocity Measurements at Jet Exit and Derivation of Swirl Number

The degree of swirl for a swirling flow is characterized by the swirl number S, the ratio of the axial flux of angular momentum to the axial flux of axial momentum, as originally proposed by Beér and Chigier[1]:

$$S = \frac{\int_0^R U W r^2 \, \mathrm{d}r}{R \int_0^R U^2 r \, \mathrm{d}r} \tag{1}$$

where U and W are the mean axial and azimuthal velocities, respectively, at the jet exit. The swirl numbers were obtained by using the measured velocities for the flow in various ranges of Reynolds number and vane angle. In this study, the controlled parameters were the Reynolds number $Re = U_m d/\nu$ and the swirl number S, where U_m is the volumetric mean axial velocity, d the diameter of the circular bluff body, and ν the kinematic viscosity of air. LDA measurements were carried out to obtain the velocity profiles at the jet exit of the annular region with $x/D = 0.09$. Figure 3 shows the results of the mean-velocity profiles of the axial, radial, and azimuthal components U, V, and W, respectively, along the radial direction at the jet exit for various Reynolds numbers and vane angles. The results show that the swirling jet flow was symmetric at the jet exit of the annular pipe. The flow rate of the swirling jet could be obtained by using the axial velocities:

$$Q = \int U \mathrm{d}A = \int_0^{2\pi} \int_0^{D/2} U r \, \mathrm{d}r \, \mathrm{d}\theta \tag{2}$$

The flow rates computed from the measured results in two radial directions were nearly the same, the difference being less than 3%. Moreover, it can be seen in Fig. 3 that the normalized axial velocities U/U_o were nearly the same. Here, U_o is the maximum axial

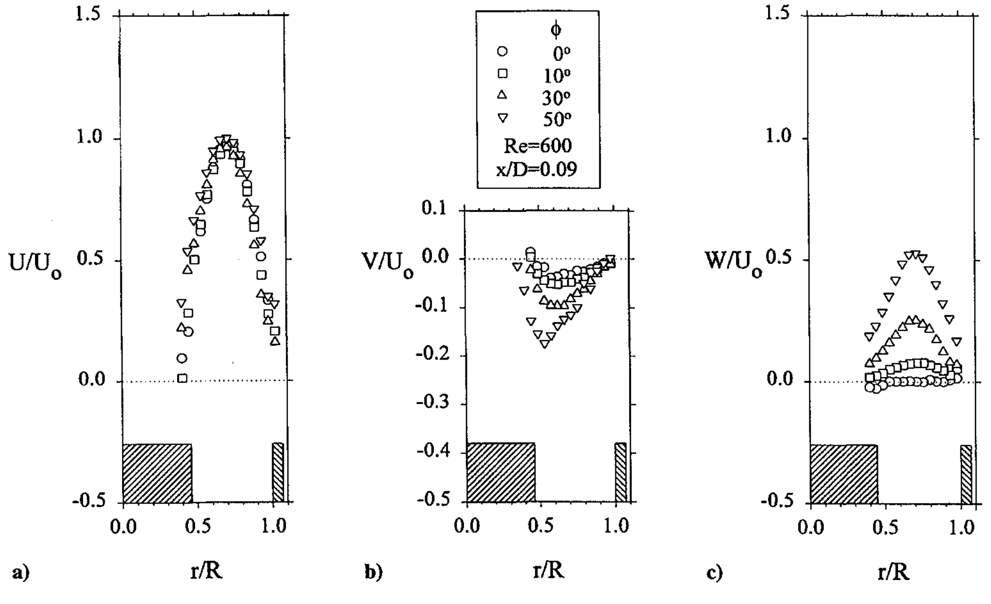

Fig. 4 LDA measurements of mean-velocity profiles at the jet exit (x/D = 0.09) for various vane angles at Re = 600 (shaded area represents geometry of the annulus): a) axial velocity, b) radial velocity, and c) azimuthal velocity.

velocity of the flow for a fixed Reynolds number and vane angle. Furthermore, Fig. 3 reveals that the swirl number is strongly dependent on the Reynolds number in addition to the vane angle in low Reynolds number cases.

The three component velocity profiles at the jet exit for a flow with $Re = 600$ and various vane angles are given in Fig. 4. The axial velocity profiles can be approximated by the same distribution. The azimuthal velocities also can be fitted by using second-order polynomials. Figure 4 also shows that the negative values of the radial velocity increase as the vane angle increases. This fact suggests that the pressure behind the bluff body decreases when the vane angle increases.

III. Results and Discussion

A. Flow Patterns

For either unconfined or confined cases, the observed flow phenomena can be classified into seven patterns. Each flow pattern is associated with a distinct region in the (Re, S) space. Figure 5 shows the regions and the corresponding flow patterns: I) stable flow, II) vortex shedding, III) transition, IV) prepenetration, V) penetration, VI) vortex breakdown, and VII) attachment. The regions for the two cases are basically the same except that regions VI and VII are separated by different boundaries. The boundary between regions VI and VII is indicated by a solid line for the unconfined case and a dotted line for the confined case.

The typical flow pattern is an open-top toroid in subregion I(a), as shown in Fig. 6a. The subatmospheric pressure in the near-wake region behind the bluff body caused the separation surface, emanating from the edge of the bluff body, to move downstream toward the central axis. Since the velocity of the annular jet was low, the subatmospheric pressure in the near-wake region was not low enough to cause a reversal of the separation surface. The center flow had to convect upstream and spread outward near the base of the bluff body; thus, some of the fluids moved downstream, but others were involved in the annular vortex. The annular vortex was clearly identified by observing the smoke traces of the vortex flow. The open-top toroid flow pattern in Fig. 7a shows a reversed axial flow near the central axis and an annular vortex around the reversed axial flow. Figure 7a also shows that the shell flow between the annular vortex and the separation surface originated from the edge of the circular bluff body. When the flow was in subregion I(b), the subatmospheric pressure was low enough to have a closed-form recirculation bubble. This flow phenomenon was due to an associated annular vortex in the central region as the swirl number reached a certain level, dependent on the Reynolds number, as shown in Fig. 6b. A schematic diagram for the closed-form recirculation bubble is shown in Fig. 7b. This flow pattern is described as a closed toroid.

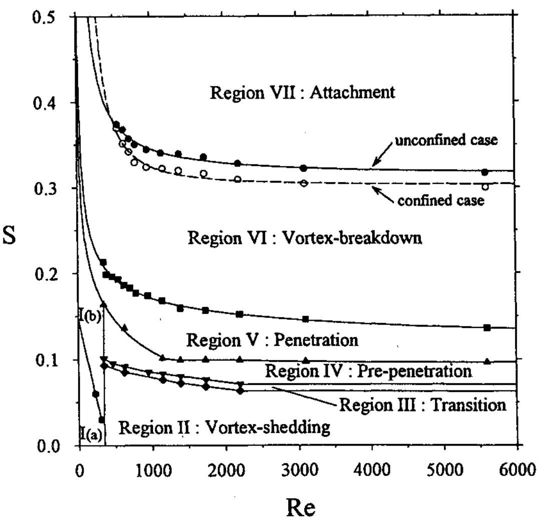

Fig. 5 Regions of the characteristic flow modes in the swirl number and Reynolds number domains for both the unconfined and the confined flow cases: region I(a), stable open-top toroid; region I(b), stable closed toroid.

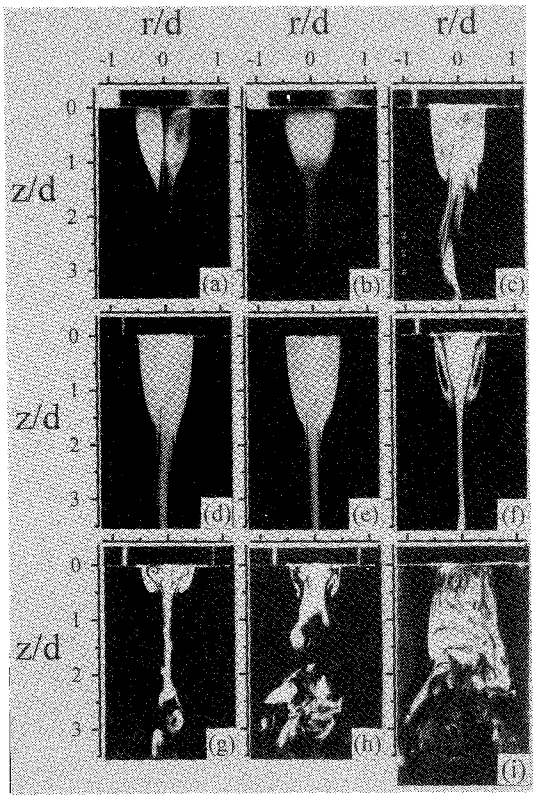

Fig. 6 Photographs of the recirculation zone behind the bluff body. For the unconfined case: a) $Re = 300$, $\phi = 0$ deg, $S = 0$; b) $Re = 300$, $\phi = 34$ deg, $S = 0.09$; c) $Re = 1400$, $\phi = 10$ deg, $S = 0.06$; d) $Re = 1400$, $\phi = 12$ deg, $S = 0.07$; e) $Re = 1400$, $\phi = 14$ deg, $S = 0.09$; f) $Re = 1400$, $\phi = 18$ deg, $S = 0.11$; g) $Re = 1400$, $\phi = 35$ deg, $S = 0.24$; and h) $Re = 1400$, $\phi = 50$ deg, $S = 0.44$ and for the confined case: i) $Re = 1400$, $\phi = 50$ deg, $S = 0.44$.

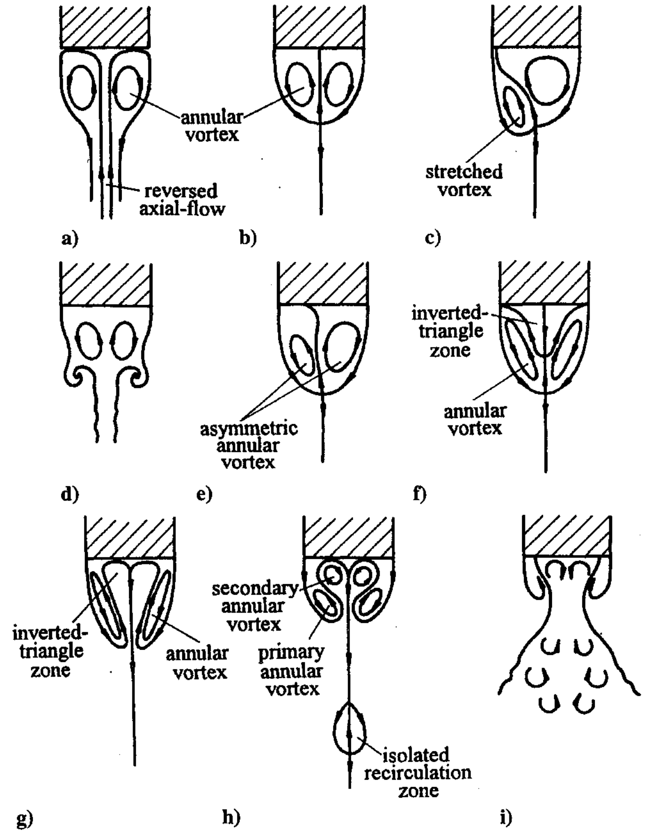

Fig. 7 Schematic diagrams of flow patterns: a) open-top toroid, b) closed toroid, c) vortex shedding, d) shear-layer vortex shedding, e) transition, f) prepenetration, g) penetration, h) vortex breakdown, and i) attachment.

In region II, asymmetric and unsteady vortex-shedding from the recirculation bubble was observed, as shown in Fig. 6c, and is called expelling vortex-shedding. The vorticity was shed from the annular vortex behind the bluff body in a form like a succession of distorted vortex loops that were not symmetric about the central axis. This asymmetric vortex-shedding is shown in Fig. 7c.

When the flow was in region III, vortex shedding disappeared; instead, an unsteady asymmetric annular vortex with a smooth boundary was observed inside the recirculation bubble. The visualization photograph in Fig. 6d, obtained by using the laser sheet, shows that the left and right sides of the asymmetric vortex cells periodically alternated. This flow phenomenon called transition is shown in Fig. 7e. The swirl number range was relatively small for the transition flow pattern.

In region IV, the vortex cells became symmetric, as shown in Fig. 6e; in other words, the three-dimensional structure of the standing annular vortex gradually became axisymmetric. An inverted-triangle zone, where the flow's axial velocity was positive, was then observed in the center of the recirculation bubble. That is, the fluids in the inverted-triangle zone inside the recirculation bubble moved downstream. However, the fluids in this zone could not penetrate the recirculation bubble when the azimuthal velocity was not high enough. This flow pattern is shown in Fig. 7f. Figure 6e also shows that there was a stagnation point with small disturbances at the apex of the inverted-triangle zone in the recirculation bubble. Those disturbances were carried upstream by the annular vortex and finally disappeared at the base of the bluff body. This region is called prepenetration.

In region V, the fluids in the central inverted-triangle zone had high enough momentum to overcome the reverse flow, which was due to the annular vortex, and the fluids could penetrate the apex of the recirculation bubble. Two equal-sized vortex cells were observed at the right and the left sides of the recirculating zone as seen in the laser-sheet photograph in Fig. 6f. The flow was thus stabilized, and this flow region is called penetration, and the flow pattern is shown in Fig. 7g.

In region VI, vortex breakdown appeared downstream from the recirculation bubble when the swirl number reached a critical value (e.g., $S = 0.16$ when $Re = 1400$). Figure 6g clearly shows the two pairs of vortex cells in the recirculating zone. The secondary annular vortex with opposite vorticity was generated between the primary annular vortex and the base surface of the bluff body; further, vortex breakdown occurred downstream, as shown in Fig. 7h. The stagnation point of the vortex breakdown moved upstream toward the recirculation bubble as the swirl strength increased. Similar observations also were made by Escudier and Keller.[10]

In region VII, the isolated recirculation zone, caused by the vortex breakdown, attached to the apex of the recirculation bubble behind the bluff body. This flow region is called attachment, as shown in Fig. 6h for the unconfined case. The observation results show evidence of a highly turbulent structure with interactions of the vortex breakdown and the annular vortices behind the central cylinder. Figure 7i shows the combination of the wake and the isolated recirculation zones.

With the same flow conditions as for Fig. 6h, the attachment phenomenon for the confined case is shown in Fig. 6i. The wake region was enlarged because of the confined effect caused by the corner recirculation zone, which is a region of subatmospheric pressure behind the sudden-expansion block. The length of the corner recirculation zone decreased as the swirl number increased after vortex breakdown had occurred. Moreover, when the flow was in the attachment region, the jet flow region expanded in the radial direction. This flow phenomenon caused the corner recirculation zone to become smaller and the central recirculation zone to become much larger, as shown in Fig. 8, than those in the other flow regions.

When the Reynolds number was higher than 1500, the velocity gradient between the freestream and the recirculating flow in the wake region behind the bluff body was larger. The shear-layer vortex shedding dominated and affected the appearance of the recirculation bubble, as shown in Fig. 7d. For $S = 0.064$ when $Re = 2200$, the flow was in the prepenetration region (Fig. 9a). The shape of the recirculation bubble was folded. Inside the recirculation bubble, the vorticity of the annular vortex increased as the Reynolds number increased. Further, the velocity gradient increased between the inverted-triangle region, with positive axial velocity, and the inner region of the annular vortex, with opposite axial velocity. Therefore, periodical disturbances, which originated from the tip of the central inverted-triangle region, were carried upstream by the reverse flow of the annular vortex and rolled up into alternatively asymmetric discrete vortices.

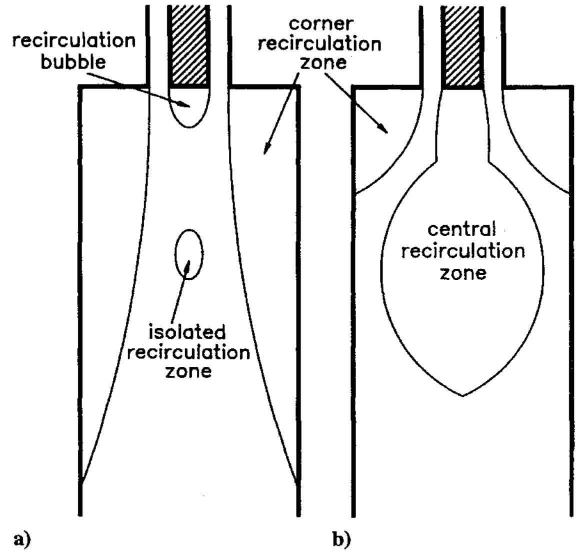

Fig. 8 Schematic diagram of the near-wake structure of a confined flow: a) vortex-breakdown region and b) attachment region.

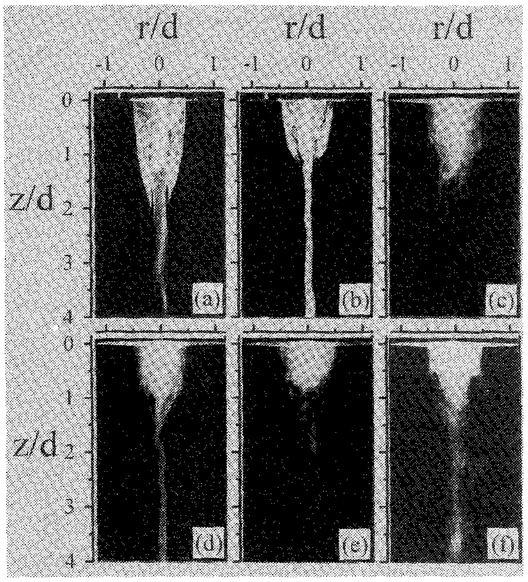

Fig. 9 Photographs of the recirculation zone behind the bluff body for unconfined cases: a) $Re = 2200$, $\phi = 10$ deg, $S = 0.064$; b) $Re = 2200$, $\phi = 20$ deg, $S = 0.13$; c) $Re = 3100$, $\phi = 15$ deg, $S = 0.09$; d) $Re = 3100$, $\phi = 20$ deg, $S = 0.13$; e) $Re = 5600$, $\phi = 15$ deg, $S = 0.09$; and f) $Re = 5600$, $\phi = 20$ deg, $S = 0.13$.

The laser-sheet photograph (Fig. 9b) for $S = 0.13$ and $Re = 2200$ reveals that the flow was in the typical penetration region. As the central flow penetrated through the recirculation bubble, the strong vorticity of the annular vortex caused the fluids near the apex of the recirculation bubble to roll up into axisymmetric discrete vortices, which moved upward between the annular vortex and the central region.

The flow could be visualized by using smoke when the Reynolds number was higher than 3000. Figures 9c and 9e show that the flow was in the prepenetration region for the conditions of $S = 0.09$ ($Re = 3100$) and $S = 0.09$ ($Re = 5600$). The results illustrate that

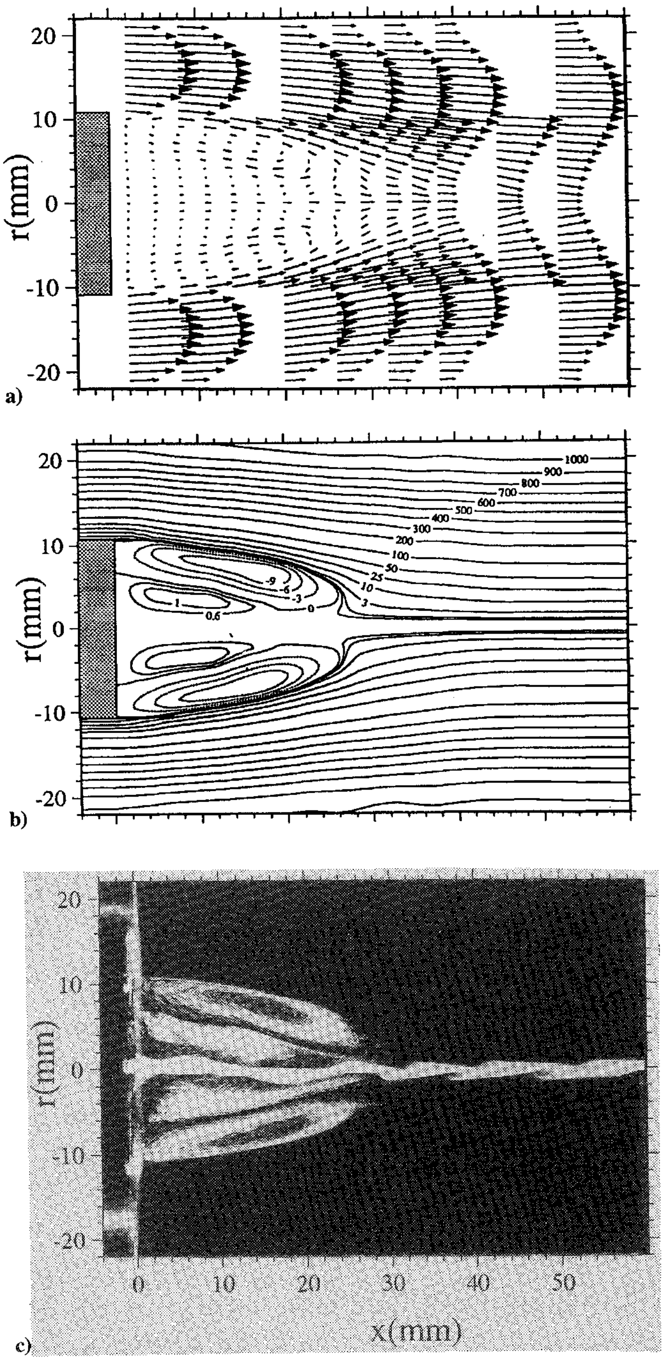

Fig. 10 Recirculation zone of an unconfined annular swirling jet with *Re* = 1200, ϕ = 20 deg, and *S* = 0.125: a) velocity vectors measured by LDA, b) calculated corresponding streamlines, and c) flow visualization picture.

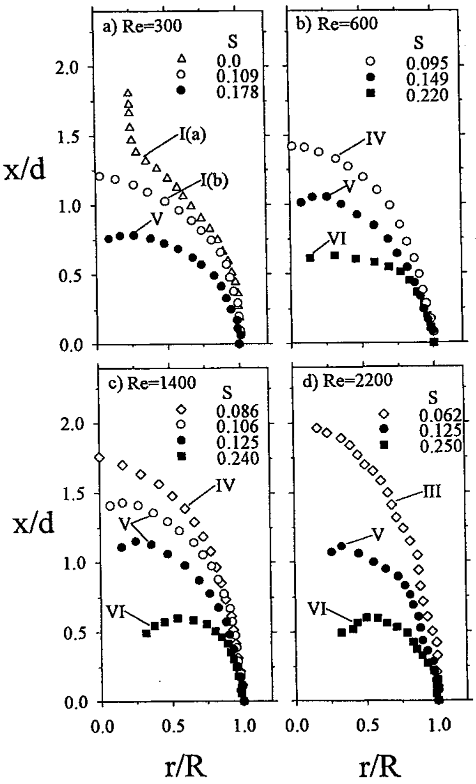

Fig. 11 Variations of the free separation surfaces under different flow conditions in the unconfined case.

the flow in the central region of the recirculation bubble was moving downward and had not yet penetrated the bubble with an unstable stagnation point. Figures 9d and 9f show that the flow was in the penetration region for the conditions of $Re = 3100$ and 5600 where $S = 0.13$.

B. Boundary of the Recirculation Zone

The time-mean velocity–vector plot of an unconfined annular swirling jet flowfield is shown in Fig. 10a for $S = 0.125$ and $Re = 1200$. The velocity vector at each location was obtained from 2000 LDA measurements for the axial and radial velocity components. The measurement results of the time-mean velocities verify that the flow was symmetric to the centerline. The flow pattern of penetration, in which an annular vortex is formed around the inverted-triangle zone where the flow has positive axial velocity, is clearly demonstrated by the corresponding streamlines. For an axially symmetric flow, the stream function is defined by

$$\psi = \int_0^r Ur\,\mathrm{d}r \tag{3}$$

The stream functions were computed from the measured axial-velocity distributions, and the lines joining the points of the constant stream function for the annular swirling jet are shown in Fig. 10b. Figure 10c reveals that the free separation surface originated from the edge of the bluff body and could be regarded as the boundary of the recirculation zone. When Fig. 10c is compared with the streamline plot in Fig. 10b, it is seen that the free separation surface coincides with the zero streamline, across which there is no net mass flow. Therefore, based on visual observation the use of the free separation surface as the boundary of the recirculation zone is reasonable.

Figure 11 gives the typical contours of the free separation surface for the flow in the regions of I(a), I(b), III, IV, V, and VI. When the swirl strength of the flow reached a critical value, the open-top toroid pattern of region I(a) changed to the closed-toroid pattern of region I(b), as shown in Fig. 11a. In prepenetration (region IV), the separation surface contracted and merged at the saddle point in the central axis to form a closed recirculation bubble (Figs. 11b and 11c). For large swirl number conditions, as in penetration and vortex breakdown (regions V and VI, respectively), the free separation surface turned toward the bluff body to form a vortex ring in the recirculation zone. Moreover, the reversal point of the separation surface moved farther upstream as the swirl number increased (Fig. 11c). Figure 11d shows that the free separation surface was not smooth since the flow had a higher Reynolds number. In regions IV and V, the contours of the separation surface could be correlated by using the dimensionless groups of x/L_r and r/R (Fig. 12). The results also show that the recirculation zones were similar for the flow in these two regions.

C. Recirculation Length

For nonswirling conditions $S = 0$, with a circular bluff body, and an area blockage ratio of 0.23, the recirculation length for both confined and unconfined flows at $Re > 350$ are shown in Fig. 13. The

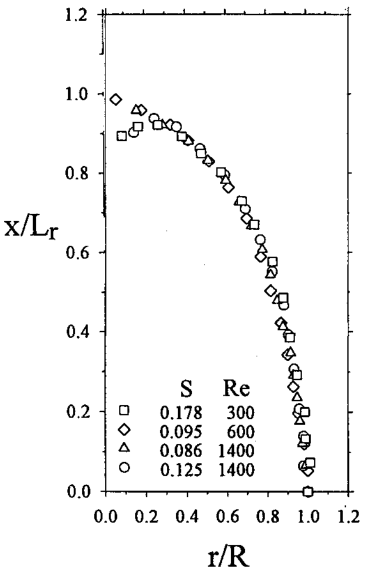

Fig. 12 Correlated contours of the free separation surfaces for the unconfined flow in the regions of prepenetration and penetration.

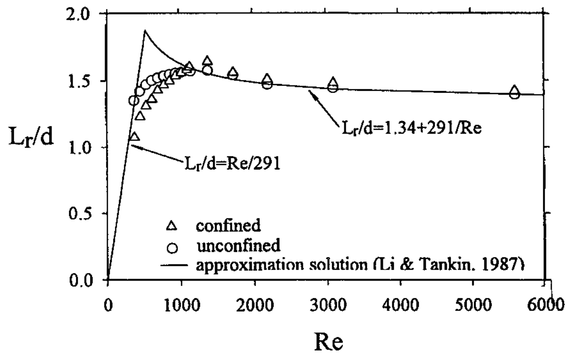

Fig. 13 Lengths of the recirculation zone L_r/d vs the Reynolds number Re for nonswirling flowfields.

solid lines in the figure represent the derived analytical solutions. When unsteady vortex-shedding occurred, the recirculation length increased nonlinearly with the Reynolds number. Furthermore, the recirculation length reached a maximum at $Re \approx 1500$ and decreased slightly thereafter when the flow was in the shear-layer vortex-shedding region. The recirculation length of the confined case was shorter than that of the unconfined case at $Re < 1000$. However, the results were opposite at $Re > 1000$.

The introduction of swirling motion into the annular jet caused the vortex-shedding phenomenon, as observed in the nonswirling case $S = 0$, to disappear when the flow was in the transition region. The recirculation bubble behind the bluff body became stable when the flow regime changed from the transition to the penetration region. Furthermore, the length of the recirculation bubble was changed under the influence of the swirling flow. Figure 14 shows the relationship between the recirculation length, L_r/d, and the swirl number for both the confined and the unconfined cases when the flow Reynolds number was 630, 1160, 2200, and 5600. When the swirl number was in the range of $0 < S < 0.07$, the recirculation length remained a constant value when the flow was in the vortex-shedding region. The recirculation length increased slightly when the flow was in the transition region, $0.07 < S < 0.08$, and reached a maximum when it was in the prepenetration region, where S was from about 0.08 to 0.1, and the annular vortex structures were axisymmetric. In the penetration region, $S > 0.1$, the fluids moved downward in the central region in the recirculation bubble and passed through the recirculating zone; the accumulated fluids in the bubble were carried outward, and this phenomenon resulted in the recirculation length becoming shorter as the swirl number increased.

To analytically estimate the recirculation length for an annular swirling jet flow, consider first a pure annular flow without swirl.

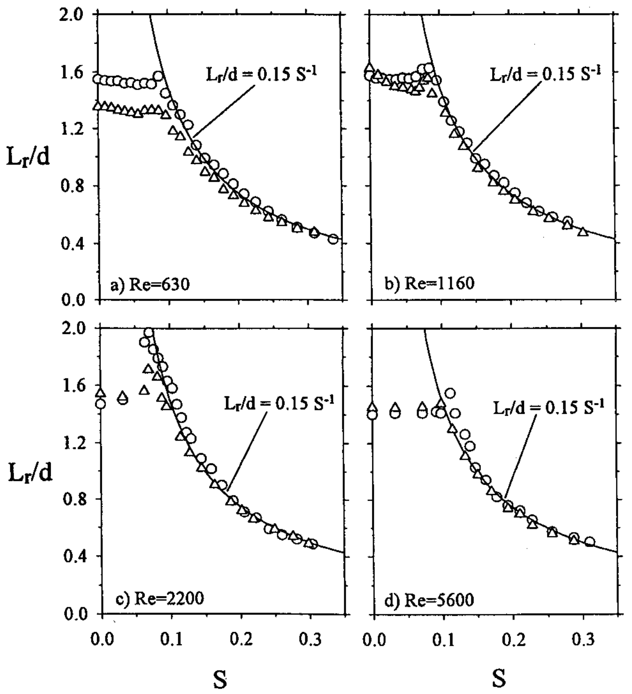

Fig. 14 Relationship between the recirculation length L_r/d and the swirl number S under different Reynolds number conditions: △, confined and ○, unconfined.

The recirculation length for a pure annular flow was found to be linearly proportional to Re (Refs. 6 and 15):

$$L_r/d = C_1 Re \tag{4}$$

for the lower Reynolds number cases ($Re < 300$), as shown in Fig. 13, where $Re = U_m(D - d)/\nu$. Since $d/D \approx 0.5$ in the present experiment, Re can be expressed as $Re = U_m d/\nu$, whereas for the higher Reynolds number cases ($Re > 10^5$), L_r/d approached a constant C_2. For an intermediate Reynolds number flow, the solution is

$$L_r/d = C_2 + 1/C_1 Re \tag{5}$$

where C_1 and C_2 are two adjustable constants. As depicted in Fig. 13, for the nonswirling flow of $S = 0$, the solid line represents the analytical solution when $C_1 = 0.0034$, and $C_2 = 1.34$ for an area blockage ratio of 0.23.

For an annular swirling jet flow, the new parameter W/U should be taken into account since the effects of the azimuthal velocity component on the flow are pronounced. Furthermore, the recirculation length was inversely proportional to W/U. In this study, the flow's azimuthal velocity in the recirculation zone was related to the mean azimuthal velocity at the jet exit. From the experiment, the ratio of the mean azimuthal and axial velocities, W_m/U_m, was proportional to the swirl number S. The experimental data reveal that S was about 0.75 times W_m/U_m, as shown in Fig. 15; thus, we can obtain

$$L_r/d = C_3/S \tag{6}$$

From the experimental results, when $S < 0.1$, the Reynolds number plays an important role in affecting the recirculation length. However, for $S > 0.1$, the Reynolds number had little effect on the recirculation length, but the swirl number had a more pronounced effect. The results of L_r/d vs S as $S > 0.1$ for both the confined and unconfined flows are shown in Figs. 16a and 16b and clearly depict the collapse of the experimental data onto a single straight line with a slope of -1. A general correlation for L_r/d vs S can then be obtained as

$$L_r/d = 0.15/S \qquad \text{for} \qquad S > 0.1 \tag{7}$$

which is consistent under various Reynolds number conditions for both the confined and unconfined cases.

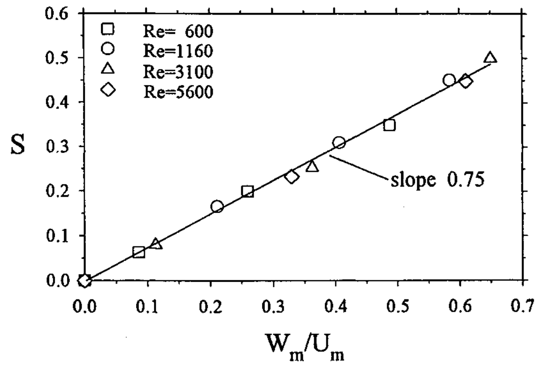

Fig. 15 Correlation of swirl number S with the ratio of the volumetric mean azimuthal velocity to the axial velocity W_m/U_m. (S, W_m, and U_m were obtained from the measured azimuthal and axial velocities at the jet exit.)

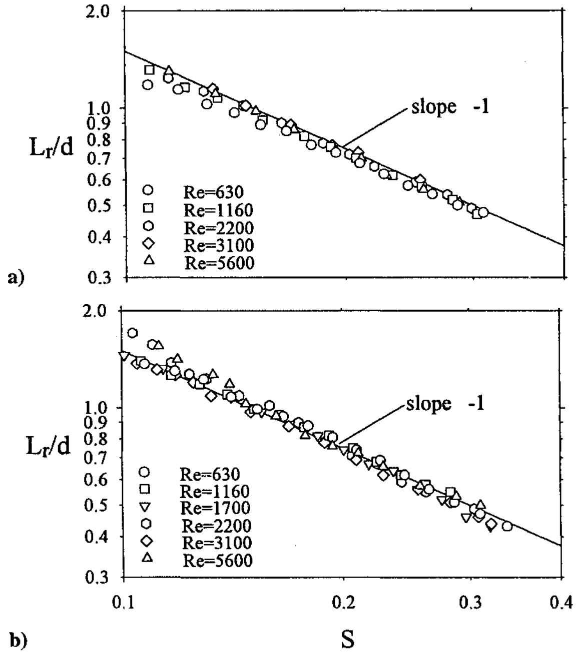

Fig. 16 Correlation of the recirculation length L_r/d vs the swirl number S: a) confined case and b) unconfined case.

IV. Conclusions

Using flow visualization by means of smoke streaks, both confined and unconfined flowfields behind an axially mounted cylindrical bluff body of an annular swirling jet have been classified into seven different flow patterns: stable flow, vortex shedding, transition, prepenetration, penetration, vortex breakdown, and attachment. The patterns are distinguished by both the swirl number S, ranging from 0 to 0.6, and the Reynolds number Re, ranging from 60 to 6000. The flow patterns and their corresponding domains in Reynolds number and swirl number for both the unconfined and the confined cases were almost the same except in the attachment regime. The recirculation bubble in the wake region stabilized in the process of transition, prepenetration, and penetration as the swirl strength increased. For both the prepenetration and the penetration regions, the contours of the free separation surface have been correlated by using the normalized parameters. In the vortex-breakdown region, the stagnation point of vortex breakdown moved upstream toward the recirculation bubble behind the bluff body when the swirl number was increased. The flow structure was called attachment when the stagnation point joined with the apex of the recirculation bubble.

The recirculation length of an annular swirling jet has been derived by using scale analysis. The results indicate that the recirculation length is inversely proportional to the ratio of the azimuthal velocity to the axial velocity. The recirculation length and the swirl number have a relationship of $L_r/d = 0.15/S$ for the flow in the region from prepenetration to vortex breakdown for Reynolds number ranging from 600 to 6000. Further, this simple relationship was independent of the flow's Reynolds number and could be applied to both the confined and the unconfined cases.

Acknowledgment

This research was supported by the National Science Council of Taiwan, Republic of China, under Grant NSC83-0401-E002-134.

References

[1] Beér, J. M., and Chigier, N. A., *Combustion Aerodynamics*, Wiley, New York, 1972.

[2] Schefer, R. W., Namazian, M., and Kelly, J., "Velocity Measurements in a Turbulent Nonpremixed Bluff-Body Stabilized Flame," *Combustion Science and Technology*, Vol. 56, Nos. 4–6, 1987, pp. 101–138.

[3] Syred, N., and Beér, J. M., "Combustion in Swirling Flows: A Review," *Combustion and Flame*, Vol. 23, 1974, pp. 143–201.

[4] Lilley, D. G., "Swirl Flows in Combustion: A Review," *AIAA Journal*, Vol. 15, No. 8, 1977, pp. 1063–1078.

[5] Taylor, A. M. K. P., and Whitelaw, J. H., "Velocity Characteristics in the Turbulent Near Wakes of Confined Axisymmetric Bluff Bodies," *Journal of Fluid Mechanics*, Vol. 139, 1984, pp. 391–416.

[6] Li, X., and Tankin, R. S., "A Study of Cold and Combusting Flow Around Bluff-Body Combustors," *Combustion Science and Technology*, Vol. 52, Nos. 4–6, 1987, pp. 173–206.

[7] Chan, W. T., and Ko, N. M. W., "Coherent Structures in the Outer Mixing Region of Annular Jet," *Journal of Fluid Mechanics*, Vol. 89, Pt. 3, 1978, pp. 515–533.

[8] Chigier, N. A., and Beér, J. M., "Velocity and Static-Pressure Distributions in Swirling Air Jets Issuing from Annular and Divergent Nozzles," *Journal of Basic Engineering*, Vol. 86, No. 4, 1964, pp. 788–796.

[9] Rhode, D. L., Lilley, D. G., and McLaughlin, D. K., "Mean Flowfields in Axisymmetric Combustor Geometries with Swirl," *AIAA Journal*, Vol. 21, No. 4, 1983, pp. 593–600.

[10] Escudier, M. P., and Keller, J. J., "Recirculation in Swirling Flow: A Manifestation of Vortex Breakdown," *AIAA Journal*, Vol. 23, No. 1, 1985, pp. 111–116.

[11] Harvey, J. K., "Some Observations of the Vortex Breakdown Phenomenon," *Journal of Fluid Mechanics*, Vol. 14, Pt. 4, 1962, pp. 585–592.

[12] Chanaud, R. C., "Observations of Oscillatory Motion in Certain Swirling Flows," *Journal of Fluid Mechanics*, Vol. 21, Pt. 1, 1965, pp. 111–127.

[13] Sarpkaya, T., "Vortex Breakdown in Swirling Conical Flows," *AIAA Journal*, Vol. 9, No. 9, 1971, pp. 1792–1799.

[14] Mueller, T. J., "Flow Visualization by Direct Injection," *Fluid Mechanics Measurements*, edited by R. J. Goldstein, Hemisphere, New York, 1983, Chap. 7.

[15] Bejan, A., *Convection Heat Transfer*, Wiley, New York, 1984.